SCIENTIFIC REPORTS

OPEN

$(Fe_{0.2}Ni_{0.8})_{0.96}S$ tubular spheres supported on Ni foam as an efficient bifunctional electrocatalyst for overall water splitting

Received: 26 March 2018
Accepted: 29 May 2018
Published online: 21 June 2018

Peiman Xu, Jingwei Li, Jiaxian Luo, Licheng Wei, Dawei Zhang, Dan Zhou, Weiming Xu & Dingsheng Yuan

Earth-abundant and efficient bifunctional electrocatalysts for both hydrogen evolution reaction (HER) and oxygen evolution reaction (OER) are highly significant for renewable energy systems. However, the performance of existing electrocatalysts is usually restricted by the low electroic conductivity and the limited amount of exposed active sites. In this work, $(Fe_{0.2}Ni_{0.8})_{0.96}S$ tubular spheres supported on Ni foam have been prepared by a sulfuration of FeNi layered double hydroxide spheres grown on Ni foam. Benefiting from the unique tubular sphere architecture, the rich inner defects and the enhanced electron interactions between Fe, Ni and S, this electrocatalyst shows low overpotential of 48 mV for HER at 10 mA cm^{-2} in 1.0 mol L^{-1} KOH solution, which is one of the lowest value of non-previous electrocatalyts for HER in alkaline electrolyte. Furthermore, assembled this versatile electrode as an alkaline electrolyzer for overall water splitting, a current density of 10 mA cm^{-2} is achieved at a low cell voltage of 1.56 V, and reach up to 30 mA cm^{-2} only at an operating cell voltage of 1.65 V.

Hydrogen energy has been regarded as the most promising alternative to replace those conventional fossil fuels due to its renewability, sustainability, high calorific value and great energy conversion with zero CO_2 emission[1–3]. Electrochemical water splitting including the cathodic hydrogen evolution reaction (HER) and the anodic oxygen evolution reaction (OER), which provides us with a feasible method for sustainable hydrogen production[4]. However, both the HER and OER are greatly limited by the high overpotential and low electrocatalytic efficiency. It is thus imperative to explore efficient electrocatalysts. At present, the most active electrocatalysts for HER and OER are Pt and RuO_2/IrO_2, respectively, but the wide-spread utilization of these catalysts is restricted by their high cost and scarcity. Therefore, enormous efforts have been made to design alternative electrocatalysts, such as transition-metal chalcogenides[5–7], phosphides[8], alloys[9], nitrides[10], carbides[11] for HER and transition-metal oxides/hydroxides[12,13], phosphates[14], borates[15] for OER. Nevertheless, most of these researches concentrate on the perfection of either HER or OER activity. In consideration of simplifying the fabrication procedures and decreasing the overall cost for water splitting system, the exploitation of efficient and low-cost bifunctional electrocatalysts for both HER and OER is highly attractive and desirable[16–21].

Transition-metal layered double hydroxides (LDHs) have exhibited efficient performance for both HER and OER, while their electrocatalytic activity is still limited by the low electronic conductivity[22–24]. Interestingly, we have noticed that the enhanced electronic conductivity and electrocatalytic performance have been achieved after converting the LDHs to transition-metal sulfides (TMSs)[25–27]. Recently, it has been confirmed that the charged states of sulfur and metals in TMSs are similar to those in hydrogenase and its analogs, which can severally as the proton-acceptors and hydride-acceptors in the water splitting processes and thereby result in efficiently catalytic activity[25]. Also, the inner defect-rich structure of TMSs has been attracting great attention because it can expose more active sites, and thus lead to outstanding improvement of electrocatalytic performance[28].

Besides, the nanostructure modification is an effective way to optimize the electrocatalytic activity[29,30]. Comparing to the solid structures of materials (nanosheets, nanoneedles, nanowires and so on), hollow micro/nanostructures have a kinetically favorable open structure, more exposed active sites and even a shortened ion

School of Chemistry and Materials Science, Jinan University, Guangzhou, 510632, People's Republic of China. Peiman Xu and Jingwei Li contributed equally to this work. Correspondence and requests for materials should be addressed to D.Y. (email: tydsh@jnu.edu.cn)

diffusion length, and thereby possess high activity for HER and OER[31–33]. Guan *et al.*[32] had fabricated CoS_2 nanotube arrays on a carbon cloth as a bifunctional electrocatalyst for overall water splitting, achieving a current density of 10 mA cm^{-2} at a cell voltage of 1.67 V. Zhang *et al.*[30] had reported the alkaline electrolyzer assembled by carbon paper/carbon tubes/cobalt-sulfide sheets electrode needed a cell voltage of 1.743 V to reach 10 mA cm^{-2}. Moreover, Chao *et al.*[33] had synthesized Co_9S_8 hollow microspheres exhibited efficiently electrocatalytic activity for OER, HER, and even the oxygen reduction reaction. In spite of these crucial advances have been done, the rational design and construction of TMSs electrocatalysts with uniquely hollow nanostructure and high performance for both HER and OER still needs more efforts.

Herein, we have prepared $(Fe_{0.2}Ni_{0.8})_{0.96}S$ tubular spheres on Ni foam ($(Fe_{0.2}Ni_{0.8})_{0.96}S$ TSs/Ni) *via* vulcanizing FeNi-LDH spheres grown on Ni foam (FeNi-LDH Ss/Ni). As expected, owing to the unique tubular sphere architecture to facilitate the release of gaseous products, the rich inner defects to expose more active sites, and the strong electron interactions between the Fe, Ni and S to improve the charge-transfer kinetics, the $(Fe_{0.2}Ni_{0.8})_{0.96}S$ TSs/Ni possesses improved performance for both HER and OER in basic electrolytes, compared with the FeNi-LDH Ss/Ni. It just needs overpotentials of 48 mV for HER and 233 mV for OER to drive a current density of 10 mA cm^{-2}. Especially, an alkaline electrolyzer assembled by the $(Fe_{0.2}Ni_{0.8})_{0.96}S$ TSs/Ni electrode can be driven by a single 1.5 V AA battery, demonstrating greatly practical prospect and feasibility for water splitting.

Experimental

Materials. $Fe(NO_3)_3{\cdot}9H_2O$ and $Ni(NO_3)_2{\cdot}6H_2O$ were purchased from Tianjin Yongda Chemical. $CO(NH_2)_2$ (urea), NH_4F, and CH_3CSNH_2 (thioacetamide) were obtained from Aladdin. Ni foam was acquired from Kunshan Electronic Limited Corporation. All chemicals were directly used as received without any purification.

Synthesis of the FeNi-LDH Ss/Ni. The Ni foam (3 cm × 3 cm) was cleaned with 3.0 mol L^{-1} HCl solution and absolute ethanol with an ultrasound for 10 min each. 484.8 mg $Fe(NO_3)_3{\cdot}9H_2O$, 872.4 mg $Ni(NO_3)_2{\cdot}6H_2O$, 303.0 mg urea and 18.5 mg NH_4F were dissolved in a solution comprised of 30 mL distilled water and 20 mL absolute ethanol under vigorous stirring for 10 min. Then, the above solution was transferred into an 80 mL Teflon-lined stainless-steel autoclave, in which contained a piece of cleaned Ni foam. The autoclave was heated at 120 °C for 6 h and allowed to cool to room temperature naturally. The product was taken out, washed with distilled water, and dried at 60 °C.

Synthesis of $(Fe_{0.2}Ni_{0.8})_{0.96}S$ TSs/Ni. Typically, 300.5 mg thioacetamide (TAA) was dissolved in a solution consisted of 40 mL distilled water and 10 mL absolute ethanol. The above solution was transferred into an 80 mL autoclave, containing a piece of as-prepared FeNi-LDH Ss/Ni. The autoclave was maintained at 140 °C for 4 h. After cooling down to room temperature, the product was taken out and severally washed with distilled water and absolute ethanol for four times. Finally, the $(Fe_{0.2}Ni_{0.8})_{0.96}S$ TSs/Ni was obtained after drying at 60 °C overnight. The mass loading is 2.5 mg cm^{-2}.

Synthesis of Ni_3S_2/Ni and FeS/Ni. The Ni-based precursor was fabricated by the analogic step as mentioned above, whereas without introducing $Fe(NO_3)_3{\cdot}9H_2O$, and altering the amount of $Ni(NO_3)_2{\cdot}6H_2O$ to 1.2 g, followed by the same sulfuration process. For FeS, the similar procedures without adding the Ni foam and replacing $Ni(NO_3)_2{\cdot}6H_2O$ with $Fe(NO_3)_3{\cdot}9H_2O$ (1.7 g) were employed. Then the FeS were bonded to a Ni foam to form FeS/Ni (see the XRD results in Fig. S1).

Characterizations. The X-ray diffraction (XRD) analysis was recorded by a MSAL-XD2 X-ray diffractometer using Cu Kα radiation (λ = 1.5406 Å). The inductively coupled plasma optical emission spectrometer (ICP-OES) was tested by Perkin Elmer Optima 2000DV. The scanning electron microscopy (SEM) observations were performed on Philips SEM-XL30S microscope operated at 15 kV. Transmission electron microscopy (TEM), high-resolution transmission electron microscope (HRTEM) and energy dispersive X-ray spectroscopy (EDS) were characterized using a JEOL JEM-2100F instrument at 200 kV. Nitrogen adsorption isotherms were recorded on a Micromeritics TriStar 3000 Analyzer at −196 °C. The Brunauer-Emmett-Teller (BET) surface area was determined by adsorption data. The X-ray photoelectron spectroscopy (XPS) measurements were carried out by using a model of ESCALab250 with an Alumina Ka (1486.6 eV) source.

Electrochemical measurements. The electrochemical measurements were performed in a conventional three-electrode setup controlled by a CHI 660D electrochemical workstation (CH Instruments, China). The as-prepared samples, Hg/HgO electrode and platinum foil were used as the working, reference, and counter electrodes, respectively. Linear sweep voltammetry (LSV) was conducted with a scan rate of 1 mV s^{-1}. All potentials in this work were converted to the reversible hydrogen electrode (RHE) according to the Nernst equation:

$$E_{RHE} = E_{Hg/HgO} + (0.098 + 0.059\ pH)\ V \quad (1)$$

Tafel plots were recorded *via* the Tafel equation:

$$\eta = b \log j + a \quad (2)$$

where η is the overpotential, b is the Tafel slope and j is the current density. Electrochemical impedance spectroscopy (EIS) experiments were performed in the frequency range from 10^5 to 0.01 Hz with an amplitude potential of 5 mV. Chronoamperometry tests were implemented at certain potentials. The double layer capacitance (C_{dl}) is proportional to the electrochemical surface area (ECSA), tested by cyclic voltammograms (CV) cycles with scanning rates of 4, 6, 8, 10, 12 and 14 mV s^{-1}. The linear slope of capacitive currents versus scan rates is equal to $2C_{dl}$[34].

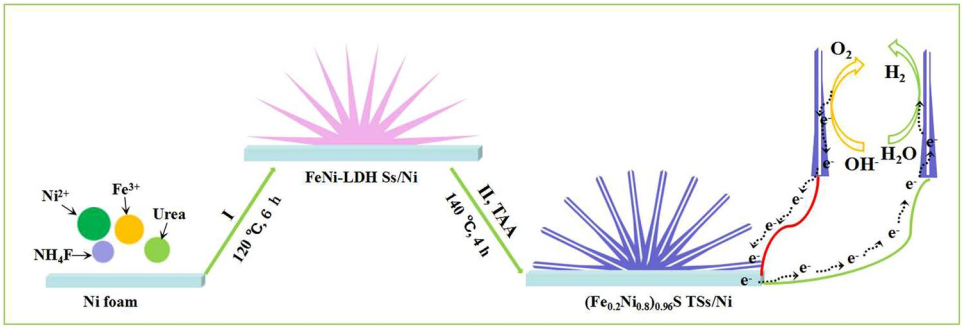

Figure 1. Schematic illustration of the synthesis of $(Fe_{0.2}Ni_{0.8})_{0.96}S$ TSs/Ni.

Results and Discussion

Structure and morphology of $(Fe_{0.2}Ni_{0.8})_{0.96}S$ TSs/Ni. Figure 1 illuminates that the $(Fe_{0.2}Ni_{0.8})_{0.96}S$ TSs/Ni has been prepared *via* two-step hydrothermal treatments. In step I, the FeNi-LDH Ss/Ni was prepared by the reactions between the metals ions and products released by the hydrolysis after heating at 120 °C for 6 h. The XRD pattern in Fig. 2a indicates the diffraction peaks at 11.4°, 23.0°, 34.4°, 39.0°, 46.0°, 59.9°, 61.3°, corresponding to the (003), (006), (012), (015), (110) and (113) planes of rhombohedral $Ni_{0.75}Fe_{0.25}(CO_3)_{0.125}(OH)_2{\cdot}0.38H_2O$ (JCPDS no. 40–0215), respectively, matching well with the typical profile of LDH materials, and the other two peaks at 44.5° and 51.8° are indexed as the (111) and (200) planes of Ni foam (JCPDS no. 65–2865). In step II, the as-prepared FeNi-LDH Ss/Ni underwent a conversion *via* a sulfur treatment at 140 °C for 4 h, using TAA as the sulfur source to synthesize $(Fe_{0.2}Ni_{0.8})_{0.96}S$ TSs/Ni. It can be seen that the diffraction peaks of FeNi-LDH are disappeared and the emerging peaks at 30.1°, 34.4°, 44.8° and 53.2° are attributed to the (100), (101), (102) and (110) planes of the hexagonal $(Fe_{0.2}Ni_{0.8})_{0.96}S$ (JCPDS no. 50–1790). ICP-OES results indicate that the atomic ratio of Fe and Ni is about 0.2: 0.8 in Table S1, further confirming the successful formation of $(Fe_{0.2}Ni_{0.8})_{0.96}S$. Moreover, the EDS spectrum suggests the coexistence of Fe, Ni, and S, while the Cu elemental comes from the copper mesh (Fig. S2).

The SEM image in Fig. S3a reveals that the FeNi-LDH spheres with a diameter of about 10 μm are uniformly grown on the surface of Ni foam. Figure S3b further shows that these spheres consist of the nanoneedles. After vulcanization, the $(Fe_{0.2}Ni_{0.8})_{0.96}S$ TSs/Ni retains the sphere characteristics of FeNi-LDH Ss/Ni, except for the enhanced surface roughness in Fig. 2b. As determined by N_2 sorption measurement (Fig. S4a), the $(Fe_{0.2}Ni_{0.8})_{0.96}S$ TSs/Ni exhibits a BET surface area of 73 $m^2\ g^{-1}$, which is larger than that of FeNi-LDH Ss/Ni (53 $m^2\ g^{-1}$). And the pore size distribution curve illustrates that both the mesopores and macropores exist in the $(Fe_{0.2}Ni_{0.8})_{0.96}S$ TSs/Ni (Fig. S4b). The internal structure of $(Fe_{0.2}Ni_{0.8})_{0.96}S$ TSs/Ni was further elucidated by TEM. Figure 2c and d show the $(Fe_{0.2}Ni_{0.8})_{0.96}S$ spheres are comprised of the nanotubes with a pore diameter of 84 nm. Notably, the formation of $(Fe_{0.2}Ni_{0.8})_{0.96}S$ tubular spheres can be explained by the Kirkendall diffusion effect[35–37]. The specific illustration is described as follows: when the solution is heated at 140 °C, it will release the S^{2-} ions from TAA. The S^{2-} will react with Fe and Ni ions to form a thin layer of $(Fe_{0.2}Ni_{0.8})_{0.96}S$ on the surface of FeNi-LDH (Fig. S5). This thin layer can be a physical barrier to impede the direct reaction of the internal FeNi-LDH and the external S^{2-} ions. Then, the outward diffusion rate of the internal Fe and Ni ions is faster than the inward diffusion rate of external S^{2-} ions, resulting in the formation of tubular sphere structure of $(Fe_{0.2}Ni_{0.8})_{0.96}S$[38,39]. In addition, the HRTEM image shows lattice fringe spacing of 0.172 and 0.202 nm in Fig. 2e, which corresponds to the (110) and (102) planes of $(Fe_{0.2}Ni_{0.8})_{0.96}S$, respectively. Significantly, compared with the FeNi-LDH Ss/Ni (Fig. S3c), abundant defects can be observed in the HRTEM image of $(Fe_{0.2}Ni_{0.8})_{0.96}S$, which may provide more enrich active sites[40], and further improve the electrocatalytic activity. The elemental mappings in Fig. 2f further indicate the homogeneous distribution of Ni, Fe and S in $(Fe_{0.2}Ni_{0.8})_{0.96}S$ TSs/Ni.

XPS analysis was employed to investigate the surface chemical states on the $(Fe_{0.2}Ni_{0.8})_{0.96}S$ TSs. As shown in Fig. S6a, the Fe 2p region displays the Fe $2p_{3/2}$ and Fe $2p_{1/2}$ peaks at 713.5 eV and 723.5 eV, respectively, indicating the Fe^{3+} oxidation states of $(Fe_{0.2}Ni_{0.8})_{0.96}S$ TSs, while another peak at 707.6 eV is assigned to Fe-S bond[26,41,42]. The Ni 2p XPS spectrum in Fig. S6b shows that the peaks at 856.1 (Ni $2p_{3/2}$) and 874.1 eV (Ni $2p_{1/2}$), as well as their satellite peaks, are assigned to Ni^{2+}, and the peak at 857.3 eV is attributed to Ni^{3+}[43]. It is worth noting that the Fe 2p and Ni 2p peaks of $(Fe_{0.2}Ni_{0.8})_{0.96}S$ TSs show a little positive shift after vulcanizing the FeNi-LDH Ss (Fig. S6a and b). Meanwhile, the spectrum of S 2p in Fig. S6c reveals the negatively shift peak at 161.6 eV with respect to the S and the peak at 162.8 eV is corresponding to the metal sulfide bonds[18,26,44]. The positive shift of Fe 2p and Ni 2p binding energy and negative shift of S 2p binding energy for $(Fe_{0.2}Ni_{0.8})_{0.96}S$ TSs are mainly attributed to the influence of electron transfer between FeNi LDH Ss and $(Fe_{0.2}Ni_{0.8})_{0.96}S$ TSs, suggesting the enhanced electron transfer from Fe, Ni to S[26,42,45]. Correspondingly, the relative interaction between Fe, Ni and S are enhanced after the sulfuration, which is beneficial to the charge transfer in the electrocatalysis process and hence favors the electrocatalytic activity.

HER electrocatalytic activity. Electrocatalytic activity of the $(Fe_{0.2}Ni_{0.8})_{0.96}S$ TSs/Ni for HER was assessed by LSV curves in a standard three-electrode system. For comparison, the FeNi-LDH Ss/Ni, 50 wt% Pt/C loading on Ni foam (50 wt% Pt/C/Ni[18], the loading of 2.5 mg cm^{-2}) and the bare Ni foam were also tested. Figure 3a shows the polarization curves of the above electrodes for HER at a scan rate of 1 mV s^{-1}. Unquestionably, 50 wt% Pt/C/Ni exhibits the best performance with an onset potential close to zero, while bare Ni foam shows almost no

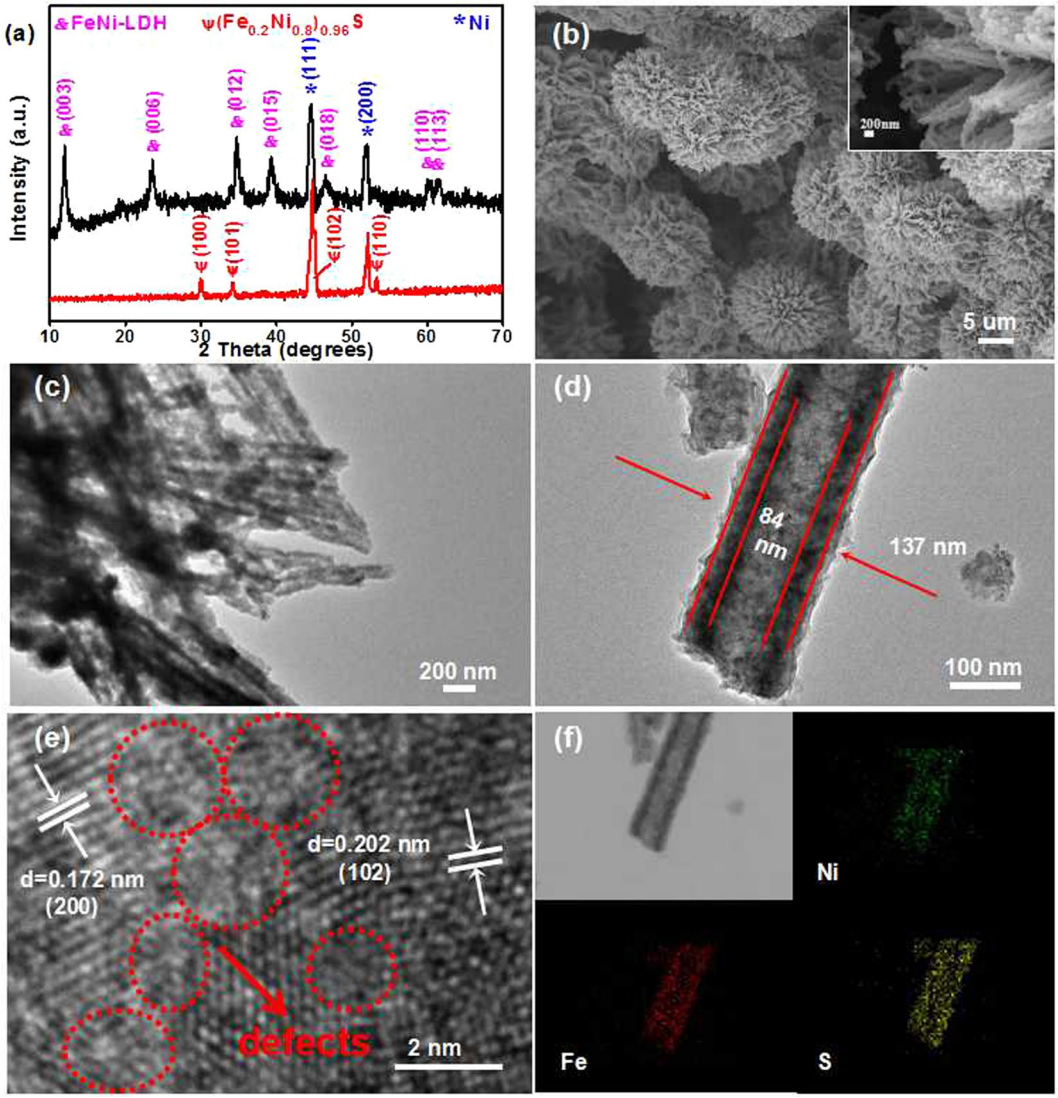

Figure 2. The characterizations of $(Fe_{0.2}Ni_{0.8})_{0.96}S$ TSs/Ni. (**a**) XRD pattern; (**b**) SEM image; (**c** and **d**) TEM images; (**e**) HRTEM image and (**f**) elemental distribution mapping.

HER performance. The as-prepared $(Fe_{0.2}Ni_{0.8})_{0.96}S$ TSs/Ni exhibits excellent HER activity with sharp increase of current density, which requires low overpotentials of 48 mV and 198 mV to deliver the current density of 10 mA cm^{-2} and 100 mA cm^{-2} ($\eta_{10} = 48$ mV, $\eta_{100} = 198$ mV), respectively, outperforming that of $\eta_{10} = 153$ mV and $\eta_{100} = 380$ mV for FeNi-LDH Ss/Ni. This result indicates the enhanced HER activity of $(Fe_{0.2}Ni_{0.8})_{0.96}S$ TSs/Ni after the sulfuration. Such excellent HER activity of $(Fe_{0.2}Ni_{0.8})_{0.96}S$ TSs/Ni is also superior to the reported noble-metal-free materials listed in Table S2.

The corresponding Tafel plots were carried out to estimate the catalytic kinetics for HER. Figure 3b shows the Tafel slope of 31.7 mV dec^{-1} for 50 wt% Pt/C/Ni is well consistent with the previous report[18]. As expected, the Tafel slope of the $(Fe_{0.2}Ni_{0.8})_{0.96}S$ TSs/Ni is 52.9 mV dec^{-1}, much smaller than that of the FeNi-LDH Ss/Ni (85.7 mV dec^{-1}), implying more favorable kinetics on $(Fe_{0.2}Ni_{0.8})_{0.96}S$ TSs/Ni. To further evaluate the charge-transfer kinetics, the EIS of $(Fe_{0.2}Ni_{0.8})_{0.96}S$ TSs/Ni and FeNi-LDH Ss/Ni was tested. As displayed in Fig. 3c, the charge transfer resistance (R_{ct}) of 0.65 Ω for $(Fe_{0.2}Ni_{0.8})_{0.96}S$ TSs/Ni is obviously lower than that of the FeNi-LDH Ss/Ni (2.79 Ω), suggesting better charge-transfer kinetics in the HER electrochemical processes. The lower charge-transfer resistance of $(Fe_{0.2}Ni_{0.8})_{0.96}S$ TSs/Ni comparing to FeNi-LDH Ss/Ni probably arises from its unique tubular sphere architecture with a shortened ion diffusion length and the optimization of electron interactions between Fe, Ni and S after the sulfuration.

Apart from the electrocatalytic activity, the stability is another key evaluating parameter to assess practical value of electrocatalysts. Therefore, the stability of $(Fe_{0.2}Ni_{0.8})_{0.96}S$ TSs/Ni was further measured by the chronoamperometric method. As shown in Fig. 3d, a stable current response suggests the $(Fe_{0.2}Ni_{0.8})_{0.96}S$ TSs/Ni maintains the electrocatalytic activity after continuing hydrogen-release for 12 h. The polarization curve of $(Fe_{0.2}Ni_{0.8})_{0.96}S$ TSs/Ni after 1000 cycles also reveals a negligible difference to the initial one (inset of Fig. 3d).

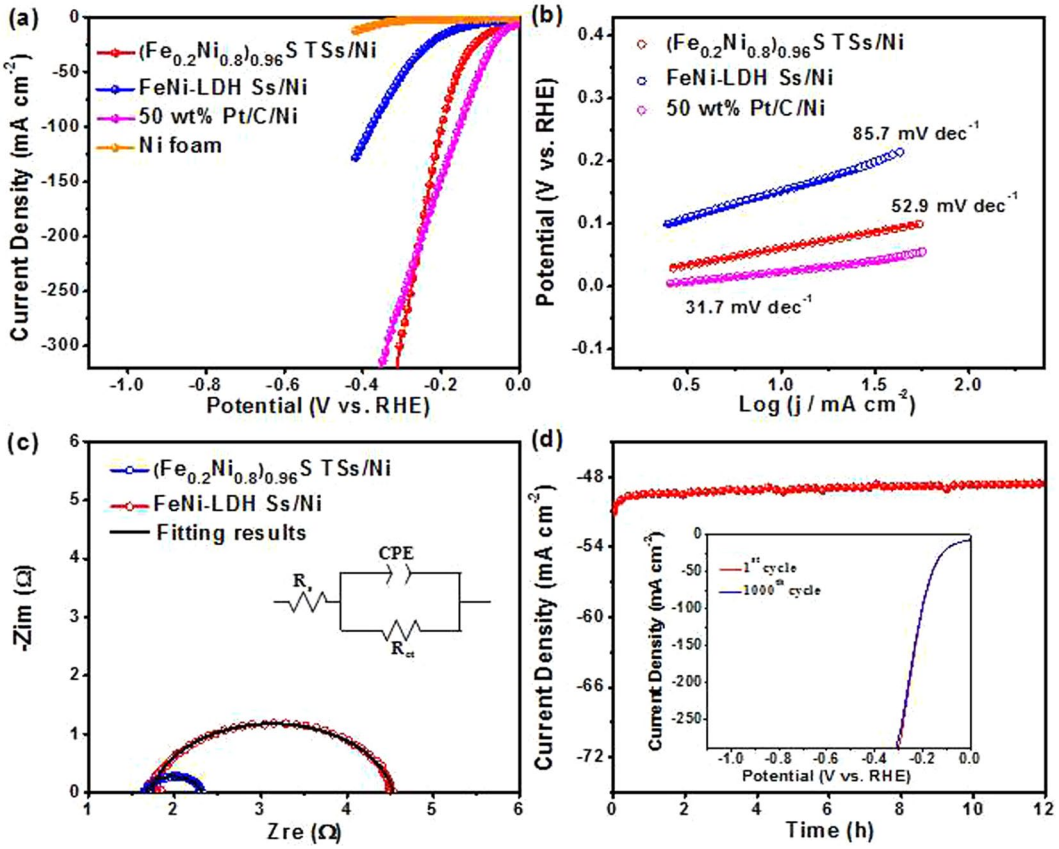

Figure 3. (**a**) Polarization curves; (**b**) Tafel plots; (**c**) Nyquist plots of $(Fe_{0.2}Ni_{0.8})_{0.96}S$ TSs/Ni, FeNi-LDH Ss/Ni measured at overpotential of 330 mV; (**d**) Chronoamperometric measurement of the $(Fe_{0.2}Ni_{0.8})_{0.96}S$ TSs/Ni at an overpotential of 154 mV. Inset is the polarization curves before and after 1000 cycles.

Further SEM images, TEM image, N_2 sorption isotherm and the corresponding pore-size distribution for $(Fe_{0.2}Ni_{0.8})_{0.96}S$ TSs/Ni after stability measurements demonstrate that this electrocatalyst is still retained their tubular sphere structure with just a little aggregation (Fig. S7).

To get insight into the inherent electrocatalytic activity of $(Fe_{0.2}Ni_{0.8})_{0.96}S$ TSs/Ni, the HER activities of Ni_3S_2/Ni and FeS/Ni were also investigated as shown in Fig. S8a. The $(Fe_{0.2}Ni_{0.8})_{0.96}S$ TSs/Ni exhibits improved HER activity comparing to the Ni_3S_2/Ni and FeS/Ni. In addition, this electrocatalyst gives a smaller Tafel slope (52.9 mV dec^{-1}) than Ni_3S_2/Ni (76.3 mV dec^{-1}) and FeS/Ni (89.7 mV dec^{-1}) (Fig. S8b). These results indicate that a significantly improved HER activity was achieved for $(Fe_{0.2}Ni_{0.8})_{0.96}S$ TSs/Ni.

OER electrocatalytic activity. The electrocatalytic activity of $(Fe_{0.2}Ni_{0.8})_{0.96}S$ TSs/Ni for OER in 1.0 mol L^{-1} KOH was further evaluated by LSV measurement at a scan rate of 1 mV s^{-1}. Figure 4a exhibits the polarization curves for $(Fe_{0.2}Ni_{0.8})_{0.96}S$ TSs/Ni, FeNi-LDH Ss/Ni, RuO_2 loading on Ni foam (RuO_2/Ni[18], the loading of 2.5 mg cm^{-2}) and the bare Ni foam. Interestingly, the anodic peak around 1.4 V vs RHE before OER can be observed for FeNi-LDH Ss/Ni, which is due to Fe and Ni species change to higher oxidation states[46,47]. However, the anodic peak of $(Fe_{0.2}Ni_{0.8})_{0.96}S$ TSs/Ni shifted negatively to 1.38 V vs RHE, which may be attributed to the improved charge transfer. Specifically, the $(Fe_{0.2}Ni_{0.8})_{0.96}S$ TSs/Ni exhibits a low η_{10} of 233 mV and an η_{100} of 310 mV for OER, superior to those of the FeNi-LDH Ss/Ni ($\eta_{10} = 263$ mV), Ni foam ($\eta_{10} = 405$ mV) and even the RuO_2/Ni ($\eta_{10} = 253$ mV). In addition, a smaller Tafel slope of $(Fe_{0.2}Ni_{0.8})_{0.96}S$ TSs/Ni (46.2 mV dec^{-1}) compares to those of FeNi-LDH Ss/Ni (63.0 mV dec^{-1}) and RuO_2/Ni (82.2 mV dec^{-1}), suggesting a more favorable OER catalytic kinetics in Fig. 4b. The lowest overpotential and smallest Tafel slope highlight the excellent performance of $(Fe_{0.2}Ni_{0.8})_{0.96}S$ TSs/Ni, which makes this uniquely tubular sphere as one of the best noble-metal-free electrocatalysts in Table S3. We further tested the OER activity for Ni_3S_2/Ni and FeS/Ni (Fig. S9a). The lowest overpotential of $(Fe_{0.2}Ni_{0.8})_{0.96}S$ TSs/Ni to reach a current density of 100 mA cm^{-2} with respect to Ni_3S_2/Ni and FeS/Ni (Fig. S9b), indicating that the synergistic effect of Ni and Fe is an effector to improve the OER activity of $(Fe_{0.2}Ni_{0.8})_{0.96}S$ TSs/Ni.

Besides, the electrochemically active surface area (ECSA) is an important parameter to understand the intrinsic activity of electrocatalysts, the double-layer capacitances (C_{dl}) is herein employed in Fig. S10. As shown in Fig. 4c, the C_{dl} of 100.1 mF cm^{-2} for $(Fe_{0.2}Ni_{0.8})_{0.96}S$ TSs/Ni is considerably larger than that of the FeNi-LDH Ss/Ni (54.4 mF cm^{-2}), revealing the existence of enriched active sites on $(Fe_{0.2}Ni_{0.8})_{0.96}S$ TSs/Ni. This is ascribed to the inner defect-rich crystal structure of $(Fe_{0.2}Ni_{0.8})_{0.96}S$ TSs/Ni. The long-term stability of $(Fe_{0.2}Ni_{0.8})_{0.96}S$ TSs/Ni for OER was tested at static potentials of 1.46, 1.50, and 1.52 V *vs*. RHE. Figure 4d shows an ignorable decrease of

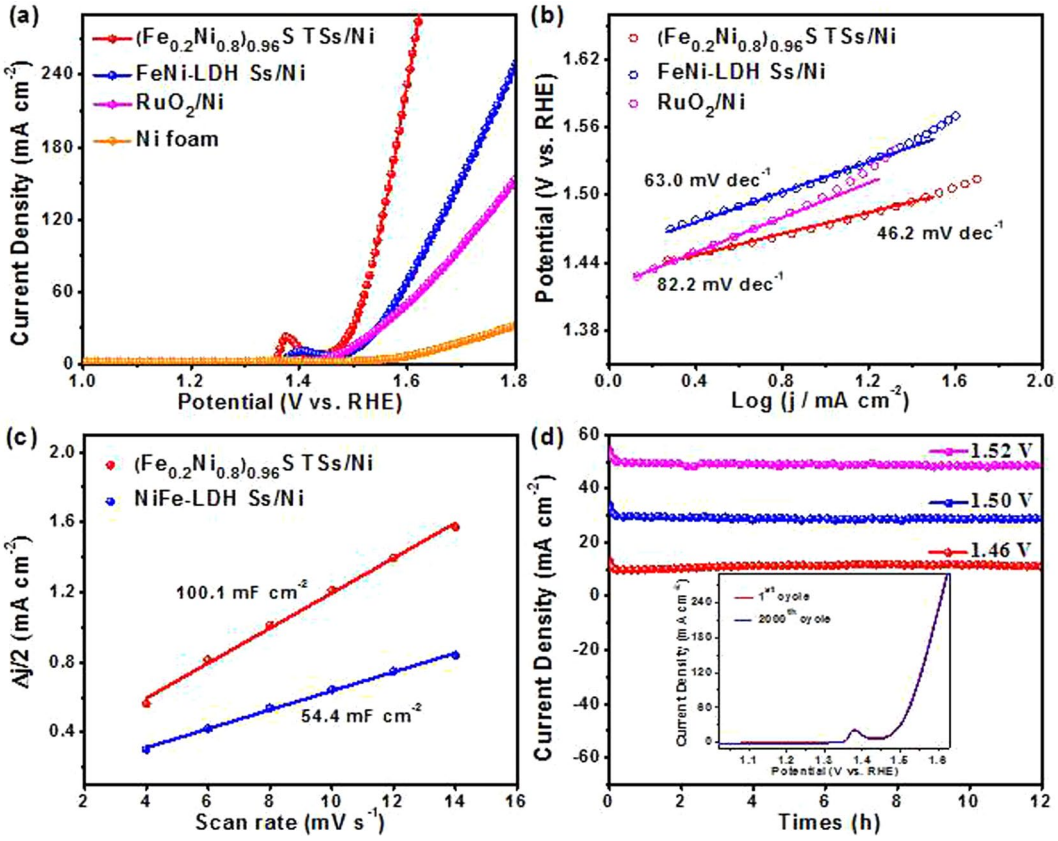

Figure 4. (**a**) Polarization curves; (**b**) Tafel plots; (**c**) Capacitive currents as a function of scan rate for $(Fe_{0.2}Ni_{0.8})_{0.96}S$ TSs/Ni and FeNi-LDH Ss/Ni. (**d**) Chronoamperometric measurements of the $(Fe_{0.2}Ni_{0.8})_{0.96}S$ TSs/Ni at different potentials. Inset is the polarization curves before and after 2000 cycles.

current density after continuing water oxidation for 12 h. The durability of $(Fe_{0.2}Ni_{0.8})_{0.96}S$ TSs/Ni is also tested by using continuous CV sweeps in 1.0 M KOH at a scan rate of 100 mV s^{-1}. The polarization curve reveals negligible degradation after 2000 cycles of CV scanning, confirming a satisfactory stability of $(Fe_{0.2}Ni_{0.8})_{0.96}S$ TSs/Ni. Similar to HER, the SEM images, TEM image, N_2 sorption isotherm and the corresponding pore-size distribution indicate the structure of $(Fe_{0.2}Ni_{0.8})_{0.96}S$ TSs/Ni is insignificant change after OER durability testing, as displayed in Fig. S11.

To further investigate the nature of $(Fe_{0.2}Ni_{0.8})_{0.96}S$ after OER performance, XPS is characterized. As shown in Fig. S12a, the sulfide peaks in the S 2p region is disappeared. The main peak at 531.7 eV in the O 1 s spectrum (Fig. S12b) indicates the oxidation of $(Fe_{0.2}Ni_{0.8})_{0.96}S$ after OER tests. Moreover, the peaks located at 711.6 eV and 721.2 eV belonged to Fe-OOH bonds in the Fe 2p region are observed and the binding energy in the Ni 2p region shows a little positive shift, as shown in Fig. S12c and d, further reveling the Ni-Fe oxo/hydroxyl species were formed on the surface of the material. These results demonstrate that the superior OER electrocatalytic activity of $(Fe_{0.2}Ni_{0.8})_{0.96}S$ could be attributable to the Ni-Fe oxo/hydroxyl species, consistent with the previous reports[26,48].

Overall water splitting. Inspired by the promising half-cell activity in HER and OER, the $(Fe_{0.2}Ni_{0.8})_{0.96}S$ TSs/Ni was further served as anode and cathode in an electrolyzer for overall water splitting. As shown in Fig. 5a, this electrolyzer just requires low cell voltages of 1.56 V and 1.65 V to drive the current density of 10 mA cm^{-2} and 30 mA cm^{-2}, respectively. Although the cell voltage of $(Fe_{0.2}Ni_{0.8})_{0.96}S$ TSs/Ni couple to generate 10 mA cm^{-2} is larger than that of the $Ni_xCo_{3-x}S_4/Ni_3S_2$/NF (1.53 V)[49], it is superior to those of FeNi-LDH Ss/Ni (1.66 V), RuO_2–50 wt% Pt/C couple (1.58 V), $NiCo_2S_4$@NiFe LDH/NF (1.60 V)[24], $Ni_{0.7}Fe_{0.3}S_2$/Ni (1.625 V)[26], $NiCo_2S_4$/NF (1.68 V)[27], CoS_2 NTA/CC (1.60 V)[33], $FeSe_2$/NF (1.73 V)[50], FeB_2-NF (1.57 V)[51], $Zn_{0.76}Co_{0.24}S/CoS_2$/TM (1.66 V)[52] and even most of the reported works exhibited in Table S4. Moreover, H_2 and O_2 with a predicted ratio of 2: 1 are obtained, and the amount of experimentally quantified gas is in good accordance with theoretically calculated gas, indicating that the $(Fe_{0.2}Ni_{0.8})_{0.96}S$ TSs/Ni affords a Faradaic efficiency of ~100% for both HER and OER (Fig. S13). Such an electrocatalyst for overall water splitting can be also powered by a 1.5 V AA battery, as shown in Fig. 5b, demonstrating the considerable potential as an alkaline electrolyzer for practical applications.

The excellent electrocatalysis performance of $(Fe_{0.2}Ni_{0.8})_{0.96}S$ TSs/Ni can be attributed to the following aspects: (1) the inner defect-rich crystal structure of $(Fe_{0.2}Ni_{0.8})_{0.96}S$ TSs/Ni can expose more effectively active sites. Meanwhile, the outer unique tubular sphere architecture of $(Fe_{0.2}Ni_{0.8})_{0.96}S$ TSs/Ni is beneficial to intimate contact between the material and electrolyte, and the release of gaseous products; (2) the change in composition between FeNi-LDH Ss/Ni and $(Fe_{0.2}Ni_{0.8})_{0.96}S$ TSs/Ni leads to strong electron interactions between Fe, Ni and S,

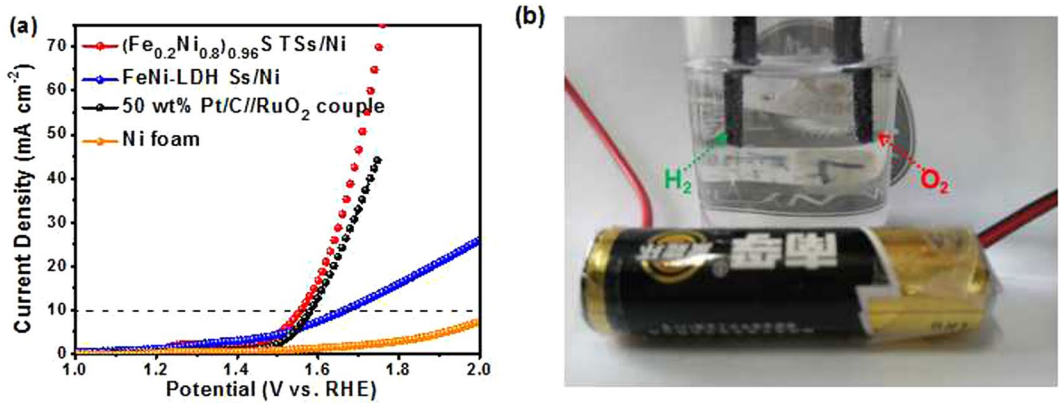

Figure 5. (**a**) Polarization curves; (**b**) photograph of $(Fe_{0.2}Ni_{0.8})_{0.96}S$ TSs/Ni couple driven by a 1.5 V AA battery. The white bubbles of H_2 and O_2 can be observed in cathode and anode, respectively.

and further optimizes charge transfer; (3) the *in-situ* growth of $(Fe_{0.2}Ni_{0.8})_{0.96}S$ TSs on Ni foam avoids the use of a binder, which can enhance the conductivity.

Conclusions

In summary, $(Fe_{0.2}Ni_{0.8})_{0.96}S$ TSs/Ni has been successfully synthesized *via* the hydrothermal sulfuration treatment of FeNi-LDH SAs/Ni. As expected, by taking advantage of the unique tubular sphere architecture, the rich inner defects and the enhanced electron interactions between Fe, Ni and S, the as-synthesized $(Fe_{0.2}Ni_{0.8})_{0.96}S$ TSs/Ni possesses higher HER and OER performance with respect to FeNi-LDH Ss/Ni. Furthermore, the alkaline electrolyzer with $(Fe_{0.2}Ni_{0.8})_{0.96}S$ TSs/Ni as the anode and cathode just needs cell voltages of 1.56 V and 1.65 V to achieve 10 mA cm^{-2} and 30 mA cm^{-2}, respectively, suggesting the great value for the practical application. More importantly, this study will encourage new opportunities to design versatile electroactive materials with a uniquely hollow structure and high performance for water splitting, fuel cells, supercapacitors, and even the batteries.

References

1. Walter, M. G. *et al.* Solar water splitting cells. *Chem. Rev.* **110**, 6446–6473 (2010).
2. Kuai, L. *et al.* A reliable aerosol-spray-assisted approach to produce and optimize amorphous metal oxide catalysts for electrochemical water splitting. *Angew. Chem.* **53**, 7547–7551 (2014).
3. Rausch, B., Symes, M. D., Chisholm, G. & Cronin, L. Decoupled catalytic hydrogen evolution from a molecular metal oxide redox mediator in water splitting. *Science* **345**, 1326–1330 (2014).
4. Li, W. *et al.* Hydrothermal synthesis of monolithic Co_3Se_4 nanowire electrodes for oxygen evolution and overall water splitting with high efficiency and extraordinary catalytic stability. *Adv. Energy Mater.* **7**, 1602579 (2017).
5. Li, R. *et al.* Nitrogen doped MoS_2 nanosheets synthesized via a low-temperature process as electrocatalysts with enhanced activity for hydrogen evolution reaction. *J. Power Sources* **356**, 133–139 (2017).
6. Li, J. *et al.* Synthesis of 3D hexagram-like cobalt-manganese sulfides nanosheets grown on nickel foam: a bifunctional electrocatalyst for overall water splitting. *Nano-Micro Lett.* **10**, 6 (2018).
7. Zhang, D. *et al.* Ni_3S_2 nanowires grown on nickel foam as an efficient bifunctional electrocatalyst for water splitting with greatly practical prospects. *Nanotechnology* **29**, 245402 (2018).
8. Yu, J., Cheng, G. & Luo, W. Hierarchical NiFeP microflowers directly grown on Ni foam for efficient electrocatalytic oxygen evolution. *J. Mater. Chem. A* **5**, 11229–11235 (2017).
9. Greeley, J., Jaramillo, T. F., Bonde, J., Chorkendorff, I. B. & Norskov, J. K. Computational high-throughput screening of electrocatalytic materials for hydrogen evolution. *Nat. Mater.* **5**, 909–913 (2006).
10. Jia, X. *et al.* Ni_3FeN nanoparticles derived from ultrathin NiFe-layered double hydroxide nanosheets: an efficient overall water splitting electrocatalyst. *Adv. Energy Mater.* **6**, 1502585 (2016).
11. Lin, H. *et al.* Cobalt-doping in molybdenum-carbide nanowires toward efficient electrocatalytic hydrogen evolution. *Adv. Funct. Mater.* **26**, 5590–5598 (2016).
12. Zhao, Y. *et al.* Graphene-Co_3O_4 nanocomposite as electrocatalyst with high performance for oxygen evolution reaction. *Sci. Rep.* **5**, 7629 (2015).
13. Jin, K. *et al.* Partially oxidized sub-10 nm MnO nanocrystals with high activity for water oxidation catalysis. *Sci. Rep.* **5**, 10279 (2015).
14. Yuan, C. Z. *et al.* Cobalt phosphate nanoparticles decorated with nitrogen-doped carbon layers as highly active and stable electrocatalysts for the oxygen evolution reaction. *J. Mater. Chem. A* **4**, 8155–8160 (2016).
15. Gupta, S. *et al.* Co-Ni-B nanocatalyst for efficient hydrogen evolution reaction in wide pH range. *App. Catal. B: Environ.* **192**, 126–133 (2016).
16. Zhang, B. *et al.* Iron-nickel nitride nanostructures *in situ* grown on surface-redox-etching nickel foam: efficient and ultrasustainable electrocatalysts for overall water splitting. *Chem. Mater.* **28**, 6934–6941 (2016).
17. Chen, P. Z. *et al.* 3D nitrogen-anion-decorated nickel sulfides for highly efficient overall water splitting. *Adv. Mater.* **29**, 1701584 (2017).
18. Chen, G. F. *et al.* Efficient and stable bifunctional electrocatalysts Ni/NixMy (M = P, S) for overall water splitting. *Adv. Funct. Mater.* **26**, 3314–3323 (2016).
19. Liu, J. *et al.* Hierarchical $NiCo_2S_4$@NiFe LDH heterostructures supported on nickel foam for enhanced overall-water-splitting Activity. *ACS Appl. Mater. Interfaces* **9**, 15364–15372 (2017).
20. Ren, J. T. & Yuan, Z. Y. Hierarchical nickel sulfide nanosheets directly grown on Ni foam: a stable and efficient electrocatalyst for water reduction and oxidation in alkaline medium. *ACS Sustainable Chem. Eng.* **5**, 7203–7210 (2017).

21. Li, R. *et al*. The urchin-like sphere arrays Co_3O_4 as a bifunctional catalyst for hydrogen evolution reaction and oxygen evolution reaction. *J. Power Sources* **341**, 250–256 (2017).
22. Zhu, X. *et al*. Monolithic-structured ternary hydroxides as freestanding bifunctional electrocatalysts for overall water splitting. *J. Mater. Chem. A* **4**, 7245–7250 (2016).
23. Wang, Z. *et al*. Coupling molecularly ultrathin sheets of NiFe-layered double hydroxide on $NiCo_2O_4$ nanowire arrays for highly efficient overall water-splitting activity. *ACS Appl. Mater. Interfaces* **9**, 1488–1495 (2017).
24. Sivanantham, A., Ganesan, P. & Shanmugam, S. Hierarchical $NiCo_2S_4$ nanowire arrays supported on Ni foam: an efficient and durable bifunctional electrocatalyst for oxygen and hydrogen evolution reactions. *Adv. Funct. Mater.* **26**, 4661–4672 (2016).
25. Ma, L. *et al*. Self-assembled ultrathin $NiCo_2S_4$ nanoflakes grown on Ni foam as high-performance flexible electrodes for hydrogen evolution reaction in alkaline solution. *Nano Energy* **24**, 139–147 (2016).
26. Yu, J., Cheng, G. & Luo, W. Ternary nickel-iron sulfide microflowers as a robust electrocatalyst for bifunctional water splitting. *J. Mater. Chem. A* **5**, 15838–15844 (2017).
27. Yang, N. *et al*. Iron-doped nickel disulfide nanoarray: A highly efficient and stable electrocatalyst for water splitting. *Nano Res.* **9**, 3346–3354 (2016).
28. Xie, J. *et al*. Defect-rich MoS_2 ultrathin nanosheets with additional active edge sites for enhanced electrocatalytic hydrogen evolution. *Adv. Mater.* **25**, 5807–813 (2013).
29. Zhang, J., Hu, Y., Liu, D., Yu, Y. & Zhang, B. Enhancing oxygen evolution reaction at high current densities on amorphous-like Ni-Fe-S ultrathin nanosheets via oxygen incorporation and electrochemical tuning. *Adv. Sci.* **4**, 1600343 (2017).
30. Wang, J., Zhong, H. X., Wang, Z. L., Meng, F. L. & Zhang, X. B. Integrated three-dimensional carbon paper/carbon tubes/cobalt-sulfide sheets as an efficient electrode for overall water splitting. *ACS Nano* **10**, 2342–2348 (2016).
31. Xiong, X. *et al*. Controlled synthesis of $NiCo_2S_4$ nanostructured arrays on carbon fiber paper for high-performance pseudocapacitors. *Nano Energy* **16**, 71–80 (2015).
32. Guan, C. *et al*. Metal-organic framework derived hollow CoS_2 nanotube arrays: an efficient bifunctional electrocatalyst for overall water splitting. *Nanoscale Horiz.* **2**, 342–348 (2017).
33. Zhang, Y. *et al*. Hierarchical Co_9S_8 hollow microspheres as multifunctional electrocatalysts for oxygen reduction, oxygen evolution and hydrogen evolution reactions. *Electrochim. Acta* **246**, 380–390 (2017).
34. Yu, J., Zhong, Y., Zhou, W. & Shao, Z. Facile synthesis of nitrogen-doped carbon nanotubes encapsulating nickel cobalt alloys 3D networks for oxygen evolution reaction in an alkaline solution. *J. Power Sources* **338**, 26–33 (2017).
35. Yin, Y. *et al*. Formation of hollow nanocrystals through the nanoscale kirkendall effect. *Science* **304**, 711–714 (2004).
36. Yin, Y., Erdonmez, C. K., Cabot, A., Hughes, S. & Alivisatos, A. P. Colloidal synthesis of hollow cobalt sulfide nanocrystals. *Adv. Funct. Mater.* **16**, 1389–1399 (2006).
37. Fan, H. J. *et al*. Influence of surface diffusion on the formation of hollow nanostructures induced by the Kirkendall effect: the basic concept. *Nano lett.* **7**, 993–997 (2007).
38. Park, G. D., Cho, J. S. & Kang, Y. C. Sodium-ion storage properties of nickel sulfide hollow nanospheres/reduced graphene oxide composite powders prepared by a spray drying process and the nanoscale Kirkendall effect. *Nanoscale* **7**, 16781–16788 (2015).
39. Tang, Y. *et al*. Synthesis of capsule-like porous hollow nanonickel cobalt sulfides via cation exchange based on the Kirkendall effect for high-performance supercapacitors. *ACS Appl. Mater. Interfaces* **8**, 9721–9732 (2016).
40. Ye, G. *et al*. Defects engineered monolayer MoS_2 for improved hydrogen evolution reaction. *Nano lett.* **16**, 1097–1103 (2016).
41. Wang, Y. *et al*. Nanoparticle-stacked porous nickel-iron nitride nanosheet: a highly efficient bifunctional electrocatalyst for overall water splitting. *ACS Appl. Mater. Interfaces* **8**, 18652–18657 (2016).
42. Jiang, J., Lu, S., Gao, H., Zhang, X. & Yu, H. Q. Ternary $FeNiS_2$ ultrathin nanosheets as an electrocatalyst for both oxygen evolution and reduction reactions. *Nano Energy* **27**, 526–534 (2016).
43. Liu, W. *et al*. Nickel-cobalt-layered double hydroxide nanosheet arrays on Ni foam as a bifunctional electrocatalyst for overall water splitting. *Dalton Trans.* **46**, 8372–8376 (2017).
44. Li, J. *et al*. Facile synthesis of CoX (X = S, P) as an efficient electrocatalyst for hydrogen evolution reaction. *J. Mater. Chem. A* **3**, 13066–13071 (2015).
45. Weng, B. *et al*. A layered $Na_{1-x}Ni_yFe_{1-y}O_2$ double oxide oxygen evolution reaction electrocatalyst for highly efficient water-splitting. *Energy Environ. Sci.* **10**, 121–128 (2017).
46. Yan, F. *et al*. Highly stable three-dimensional nickel-iron oxyhydroxide catalysts for oxygen evolution reaction at high current densities. *Electrochim. Acta* **245**, 770–779 (2017).
47. Wang, Z. *et al*. Porous Nickel-Iron Selenide Nanosheets as Highly Efficient Electrocatalysts for Oxygen Evolution Reaction. *ACS Appl. Mater. Interfaces* **8**, 19386–19392 (2016).
48. Zhu, W. *et al*. Nickel sulfide microsphere film on Ni foam as an efficient bifunctional electrocatalyst for overall water splitting. *Chem. Commun.* **52**, 1486–1489 (2016).
49. Wu, Y. *et al*. Efficient electrocatalysis of overall water splitting by ultrasmall NixCo3-xS4 coupled Ni_3S_2 nanosheet arrays. *Nano Energy* **35**, 161–170 (2017).
50. Panda, C. *et al*. From molecular 2Fe-2Se precursor to $FeSe_2$ acting as highly efficient electrocatalyst for overall water-splitting. *Angew. Chem. Int. Ed.* **56**, 10506–10510 (2017).
51. Li, H. *et al*. Earth-abundant iron diboride (FeB_2) nanoparticles as highly active bifunctional electrocatalysts for overall water splitting. *Adv. Energy Mater.* **7**, 1700513 (2017).
52. Liang, Y. *et al*. $Zn_{0.76}Co_{0.24}S/CoS_2$ nanowires array for efficient electrochemical splitting of water. *Electrochim. Acta* **190**, 360–364 (2016).

Acknowledgements

This work was supported by National Natural Science Foundation of China (21376105 and 21576113).

Author Contributions

Peiman Xu, Jingwei Li and Dingsheng Yuan conceived the idea. Peiman Xu and Jingwei Li did the major part of experiments and co-wrote the manuscript. Jiaxian Luo and Dawei Zhang conducted the electrochemical tests. Licheng Wei and Dan Zhou performed SEM and TEM characterizations. Weiming Xu involved in discussion and prepared the figures. All the authors read and corrected the manuscript.

Additional Information

Supplementary information accompanies this paper at https://doi.org/10.1038/s41598-018-27477-z.

Competing Interests: The authors declare no competing interests.

Publisher's note: Springer Nature remains neutral with regard to jurisdictional claims in published maps and institutional affiliations.